Low-cost data logging device to measure irradiance based on a Peltier cell and artificial neural networks

E Palo-Tejada[1]*, V Campos-Falcon[1], M Merma[1] and E Huanca[2]

[1]Universidad Nacional de San Agustín de Arequipa, Peru

[2]Department of Electric and Electronic Engineering, Universidad Católica San Pablo, Arequipa, Peru

*Email: jpalot@unsa.edu.pe

Abstract. The measurement of solar irradiance is one of the most important variables for ensuring working conditions at maximum power (MPPT) in a photovoltaic system (PV). In this work, a pyranometer is constructed to measure solar irradiance using a Peltier cell as a thermoelectric generator (TEG), an absolute temperature sensor and a feedforward neural network. The instrument is a low-cost data logger that runs on 3 AAA batteries, has an autonomy of up to 1 year and can record up to 65 000 irradiation data points at programmable time intervals.

1. Introduction

The growing demand for energy and the increasing concern for the environment have increased the interest in renewable energy generation with low environmental impact. Among these technologies, photovoltaic generation is undoubtedly the fastest growing type. New photovoltaic technologies have been introduced, such as Passivated Emitter and Rear Cell (PERC), "Heterojunction with Intrinsic Thin layer (HIT) Solar Cell" and "Copper indium gallium selenide (CIGS) Solar Cells. In upcoming years, they will lead to a change in the energy matrix of countries that have abundant solar resources [1-6].

To guarantee the optimal operation of photovoltaic installations, measurement of the irradiance is one of the most important factors. In large photovoltaic parks, the irradiances on the photovoltaic arrays are not the same on the photovoltaic panels that integrate them; for example, by the effects of clouds, aerosols in the atmosphere, dust, and so on. To guarantee MPPT conditions in the PV panel, it is necessary to distribute adequately the matrix of irradiance meters, and according to the International Standard ISO 9060 and the World Meteorological Organization (WMO), a pyranometer can be used as an instrument designed to measure global or diffuse solar radiation.

The operating principle of a pyranometer is based on the thermoelectric effect. The transducer is a passive thermal sensing element called a thermopile, and it is built with a large number of electrically connected thermocouples in series. The absorption of thermal radiation by one of the thermocouple joints, called a hot joint, increases its temperature. The differential temperature between the active junction and the cold junction, maintained at a fixed temperature, produces an electromotive force that is directly proportional to the differential temperature. The temperature difference between the hot and

cold face of the thermopile is converted into a voltage that is a linear function of the absorbed solar irradiance [7].

Instruments that use thermopiles as a sensing element are accurate but expensive, which is why many low-cost devices for irradiance measurements have been proposed. For example, in [8], a photovoltaic panel is used as a sensing element, and an approach is taken based on the analytical expressions of the "single diode" circuit model for a silicon photovoltaic device, where the maximum power current and panel temperature are measured, to estimate the irradiance. In [9], the authors use a photovoltaic panel and Artificial Neural Networks (ANN) embedded in an 8 bit microcontroller to estimate the irradiance from the short-circuit current and temperature of the photovoltaic module that is used as a sensor. In [10], the effect of changes in the spectral distribution of the incident solar radiation on the direct normal response capability of a photodiode pyranometer is studied. In [11], they use an LDR photoresistor and an ANN to estimate the irradiance from measured resistance and temperature values taken from the LDR.

A Peltier TEC-12705 cell, which is commonly marketed for thermoelectric chiller (TEC) applications, in this work takes advantage of the Seebeck effect. The Peltier is used as a thermoelectric generator (TEG); an LM35 semiconductor temperature sensor, artificial neural networks and an 8-bit microcontroller are also used, to measure the cold face temperature and the open circuit voltage in the Peltier cell and to estimate the irradiance. The results are compared with one of the best thermopile-based instruments available in the market.

2. Peltier cell pyranometer

The parts that make up the pyranometer are shown in Figure 1. In this work, a Peltier cell '4' TEC1-12705 is used as a sensor element. The hot face of the Peltier cell is coated with a black low emissivity paint that is exposed to sunlight through an optical glass dome '2', which is mounted on a fiberglass ring '3'. The cold side of the Peltier cell is in contact with a thermal mass of aluminum '5', which is maintained at room temperature thanks to the '1' protector made of acrylic and which is subjected to the thermal mass by three '6' supports. Inside the thermal mass, there is a space where the electronics, the batteries and the desiccant are installed. Part '7' is a nylon cover that is screwed onto the aluminum body of the instrument, with 3 '8' brackets to level the pyranometer.

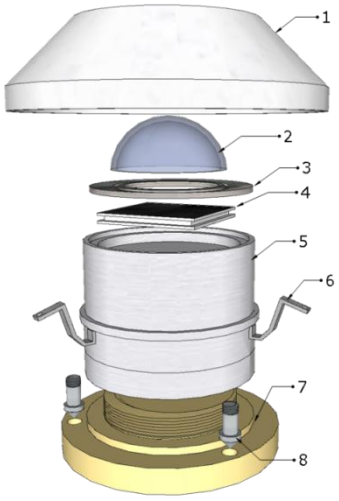

Figure 1. Parts of the Peltier cell pyranometer.

When the instrument is exposed to sunlight, the configuration shown in Figure 1 maintains a temperature gradient between the cold face and the hot face (black body) of the Peltier, and according to the equation $V_{oc} = \alpha(T_h - T_c)$, there is a potential difference that is proportional to the temperature delta and the thermoelectric potential of the material.

The temperature T_c of the cold face of the Peltier is measured using a semiconductor sensor LM35, and the open circuit potential VOC is measured with the appropriate instrumentation. The signals are delivered to a neural network that was previously trained with a Class A CMP22 Flat spectral pyranometer from KIPP & ZONEN.

(A) (B) (C)

Figure 2. (A) Peltier pyranometer, (B) model, (C) internal view.

Between the nylon cover and the aluminum body of the pyranometer, as seen in figure 2-C, there is a space to house the electronic circuit shown in figure 2. The Peltier cell '1' and the temperature sensor '2' are connected to the 8 bit microcontroller '9' through an analogue adapter circuit that delivers a digital signal encoded in 12 bit. A real-time clock '8' and an eeprom memory '5' are connected to the microcontroller. Communication of the circuit with the outside is accomplished through the USB connector '3', which also serves to recharge the battery '7' through the power management circuit '6'.

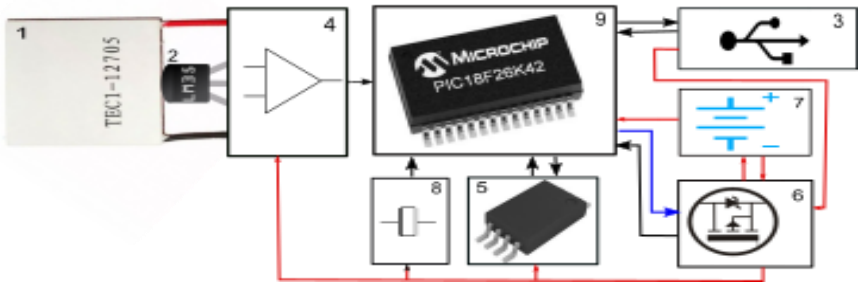

Figure 3. Peltier cell pyranometer electronic hardware.

The embedded system software includes the neural network, which allows recording irradiance data from the measured data of the open circuit voltage and temperature of the cold face of the Peltier cell. The software also resolves everything related to communication, battery power management and the real-time clock, which allows recording data at intervals configurable by USB. The minimum time between data is 1 s. The power management circuit allows a battery autonomy of up to 1 year, which depends on the sampling rate. The instrument can record up to 65 000 irradiance data points, dates and times.

3. Dependence of the open circuit voltage on the temperature on the cold face

As shown in [12-17], the open circuit voltage of the Peltier cell is given by $V_{oc} = \alpha(T_h - T_c)$, with $\alpha = \frac{1}{eT}\frac{L_{12}}{L_{11}}$, to experimentally show the dependence on V_{oc} with respect to the absolute temperature of the cold face (which is in contact with the thermal mass of aluminum). When measuring and recording the irradiation $G_{K\&Z}$ with PK&Z, the result is shown in figure 4-B. Note that the irradiance reaches $16\,00\ W/m^2$ because of cloudy weather, The open circuit voltage V_{oc} and the temperature T_c of the cold face in the Peltier pyrometer are measured. The results are shown in Figure 4-A; the black voltage reaches 0.5 V, and the blue temperature reaches 35 ° C.

As a first approximation, it is assumed that the irradiance and voltage V_{oc} are linearly related according to $G_{PLN} = B_0 + B_1 \cdot V_{oc}$. In Figure 4-C, the irradiance is drawn as a function of the open circuit voltage V_{oc}, and least squares are used to find the constants B_0 and B_1. Figure 4-D shows the estimated irradiances G_{PLN} found from V_{oc} and the measured irradiance $G_{K\&Z}$ as a function of time for a new data set. The discrepancy between these values is especially evident for the irradiance values plus high and low.

The difference $G_{K\&Z} - G_{PLN}$ in blue and the temperature of the cold face of the black Peltier is shown in Figure 4-E. This difference is finally plotted as a function of temperature, and the results are shown in Figure 4- F. It is verified that the difference between G_{PLN} and $G_{K\&Z}$ has a clear dependence on the absolute temperature of the cold face of the pelier cell

Therefore, it is concluded that any model that attempts to determine the irradiance from V_{oc} must incorporate the absolute temperature of the cold face of the Peltier. Two approaches are proposed to compensate for the influence of the absolute temperature on the cold face: multiple linear regression and artificial neural networks.

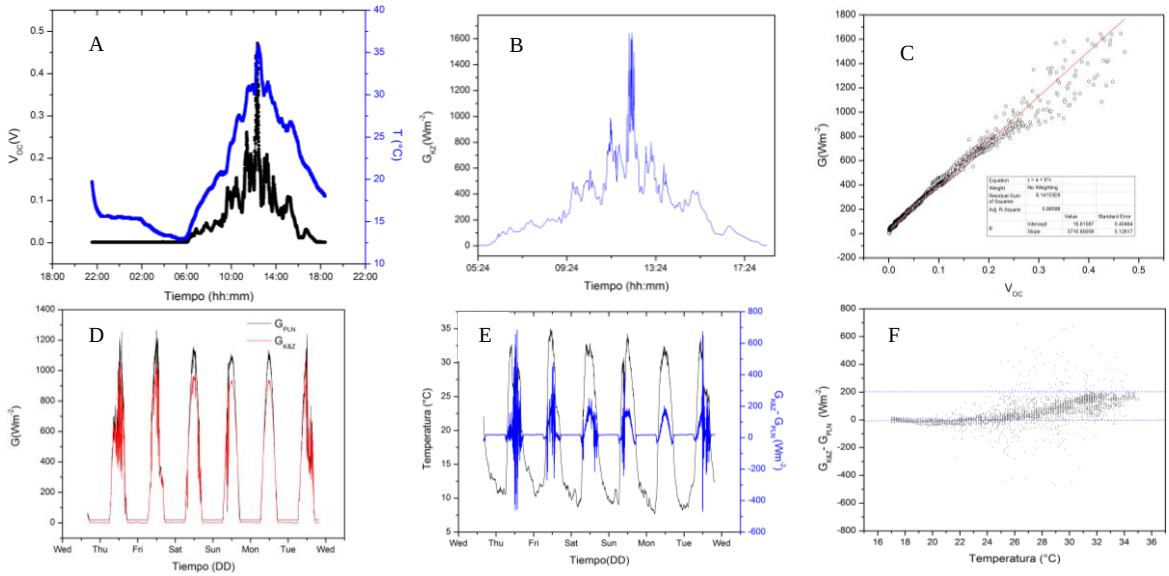

Figure 4. (A) Open circuit voltage and cold face temperature of the Peltier pyranometer. (B) Irradiance measured with the K&Z pyranometer. (C) Irradiance measured as a function of the open circuit voltage. (D) Irradiance measured and irradiance estimated (E) Difference between the estimated irradiance and the irradiance measured D) Dependence of the difference between the irradiance measured and that estimated with the temperature.

4. Experimental data

To implement the multiple linear regression procedure and artificial neural networks, the experimental data set shown in Figure 5 is used. The graphs on the left of 5-A and 5-B show the temperature data of the cold face, T_C and the open circuit voltage, V_{oc} of the Peltier. Note that the temperature is in the range $10°C < T_C < 35°C$ and the voltage is $0\ mV < V_{oc} < 350\ mV$. As seen in figure 5-C and 5-D, the irradiance measured with the pyranometer K&Z under clear sky conditions reaches $G_{K\&Z} = 1\,000\ (W/m^2)$, and in conditions of partial cloudiness, it measures $G_{K\&Z} = 1\,200\ (W/m^2)$.

This set of experimental data will be used indistinctly to calculate the parameters of the multiple linear fit and to train the neural network and test both models.

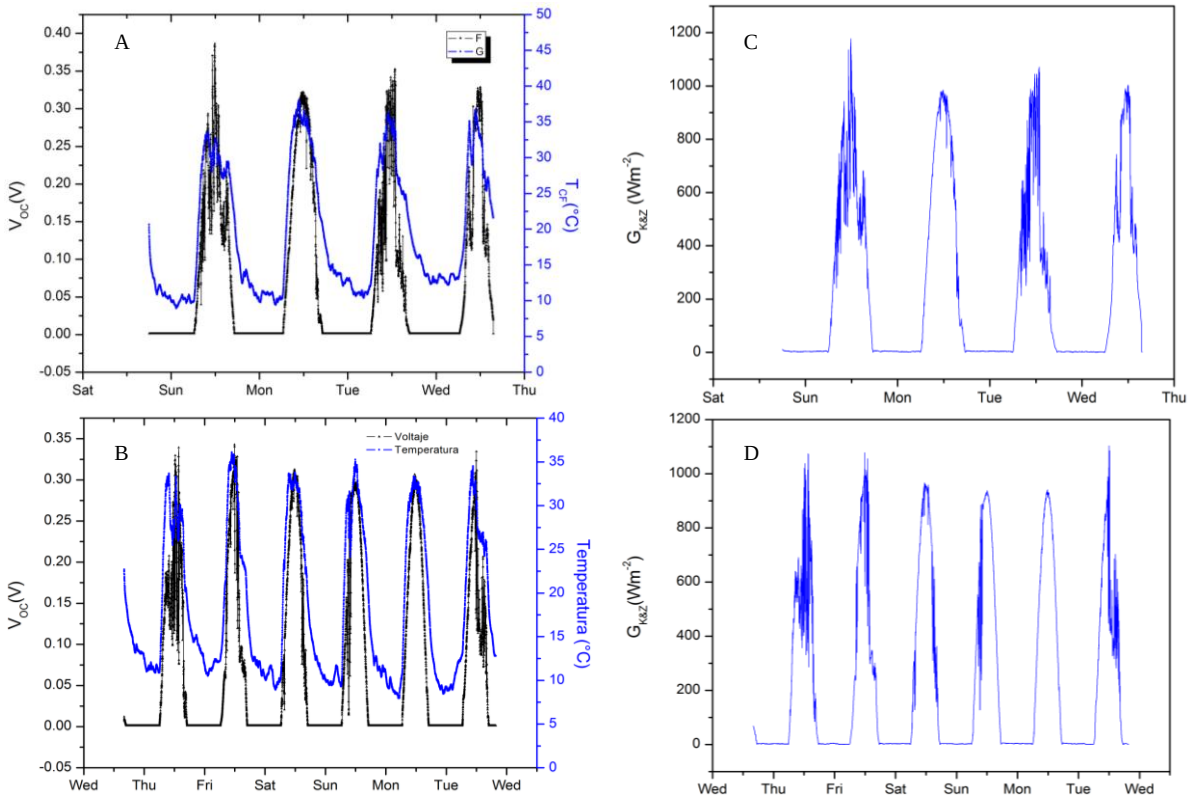

Figure 5 Right, data from V_{oc} y T_C of the pyranometer PLT; left, data of $G_{K\&Z}$ taken with the pyranometer K&Z registered at a rate of 10 (s)

5. Comparison of models and analysis of statistical errors

To evaluate the performance of the proposed models, multiple regression and artificial neural networks, the measured irradiance with the K&Z pyranometer is compared with the estimated irradiance from the values of V_{oc} and T_c delivered by the PLT pyranometer. Here, 4 statistics are used [18]: the mean absolute error MAE, mean square error $RMSE$, mean absolute percentage error $MAPE$ and determination coefficient R^2.

6. Multiple regression to compensate for the absolute temperature dependence

The irradiance $G_{PLT} = G_{PLT}\,(V_{oc}, T_c\,, V_{oc} \cdot T_c)$ is estimated from measured data of the open circuit voltage and cold face temperature, according to the model shown in equation (1).

$$G_{PLT} = B_1 + B_2 \cdot V_0 + B_3 \cdot T_c + B_4 \cdot V_0 \cdot T_c \tag{1}$$

For the calculation of the adjustment parameters $B = [B_1\ B_2\ B_3\ B_4]$, the experimental data of the open circuit V_{oc} and the temperature T_c in the X matrices and the irradiance data measured with the $K\&Z$ pyranometer, in the matrix Y, are ordered as shown in equation (2). Note that matrix X has an additional column of unit terms, due to the existence of the independent adjustment parameter B_1.

$$\mathbf{X} = \begin{bmatrix} 1 & \mathrm{V_{oc}^1} & \mathrm{T_c^1} & \mathrm{V_{oc}^1 \cdot T_c^1} \\ 1 & \mathrm{V_{oc}^2} & \mathrm{T_c^2} & \mathrm{V_{oc}^2 \cdot T_c^2} \\ \vdots & \vdots & \vdots & \vdots \\ 1 & \mathrm{V_{oc}^N} & \mathrm{T_c^N} & \mathrm{V_{oc}^N \cdot T_c^N} \end{bmatrix} \qquad \mathbf{Y} = \begin{bmatrix} \mathrm{G_{K\&Z}^1} \\ \mathrm{G_{K\&Z}^2} \\ \vdots \\ \mathrm{G_{K\&Z}^N} \end{bmatrix} \tag{2}$$

Adjustment parameters B are found by solving the vector expressed system of equations shown in equation (3). The results are shown in table 1.

$$\mathbf{B} = [\mathbf{X}'\mathbf{X}]^{-1}\mathbf{X}'\mathbf{Y} \tag{3}$$

Table 1. Parameters B from multiple regression to a plane.

B_1	B_2	B_3	B_4
$W \cdot m^{-2}$	$W \cdot V^{-1} \cdot m^{-2}$	$W \cdot °C^{-1} \cdot m^{-2}$	$W \cdot V^{-1} \cdot °C^{-1} \cdot m^{-2}$
-58.0	3 819.8	4.9	31.8

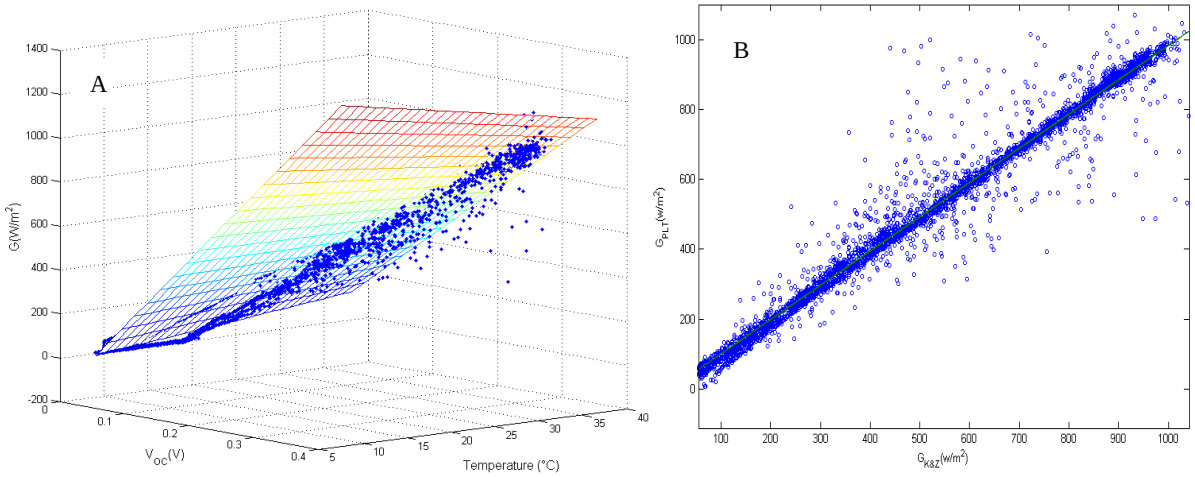

Figure 6. On the left, the multiple regression plane. On the right graph, the irradiance $G_{PLT} = G_{PLT}\,(V_{OC}, T_C, V_{OC} \cdot T_C)$ measured with the Peltier pyranometer against the irradiance $G_{K\&Z}$ measured with the pyranometer $K\&Z$.

The results of the multiple regression to a plane are shown in Figure 6-A. Most of the experimental points are in the adjustment plane. In Figure 6-B, the irradiance $G_{K\&Z}$ measured with the pyranometer is plotted against the irradiance estimate delivered by the Peltier pyranometer, and using the regression coefficients shown in Table 1, the model is written as follows:

$$\mathrm{G_{PLT}} = -58.0 + 3\,819.8 \cdot \mathrm{V_0} + 4.9 \cdot \mathrm{T_c} + 31.8 \cdot \mathrm{V_0} \cdot \mathrm{T_c} \tag{4}$$

The statistics of the comparison between the measured and estimated data are shown in table 2. Figure 7-A shows the irradiance measured with the $K\&Z$ pyranometer and Peltier for 7 consecutive days. Figure 7-B shows the irradiance result for Thursday. In general, the model $G_{PLT} = G_{PLT}\,(V_{OC}, T_C, V_{OC} \cdot T_C)$ estimates the irradiance quite well, except for very high or very low values. Figure 7 also includes the results of the estimated irradiance with $G_{PLN} = G_{PLN}\,(V_{OC})$, where the temperature T_c is not included. In this case, significant errors are made over the entire irradiance range.

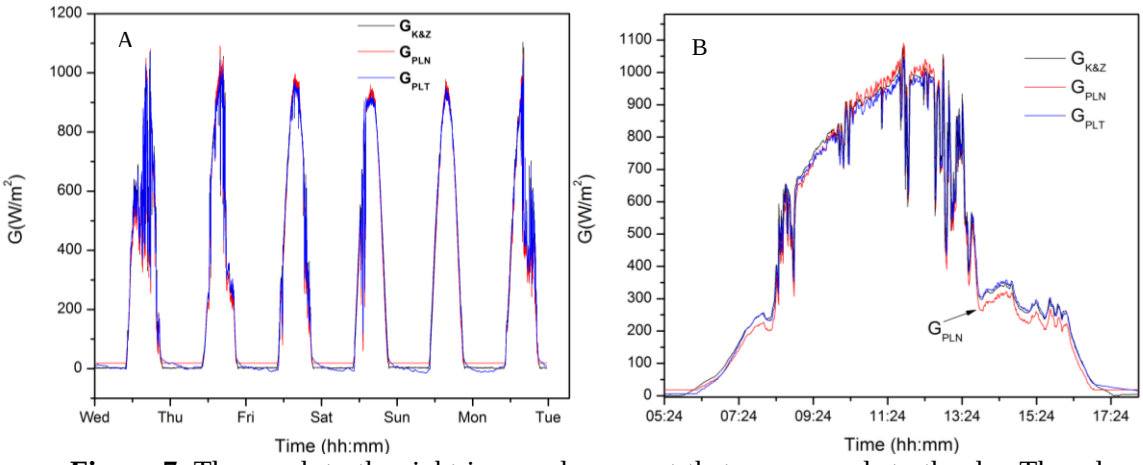

Figure 7. The graph to the right is an enlargement that corresponds to the day Thursday. In the graph to the left, the figure shows the irradiance $G_{K\&Z}$ measured by the pyranometer K&Z and the irradiance with the pyranometer Peltier, without considering the temperature $G_{PLN} = G_{PLN}(V_{oc})$ and considering the temperature and $G_{PLT} = G_{PLT}(V_{OC}, T_C, V_{OC} \cdot T_C)$

Table 2. Multiple Fit to a Plane Statistics

MAE	RMSE	R^2	MAPE
$W \cdot m^{-2}$	$W \cdot m^{-2}$	--	%
27.1993	54.7348	0.9647	0.0744

In multiple adjustment to one plane, the determination coefficient R^2 indicates that 96% of the measured data can be explained by the model. A visual approximation of that indicated can be observed in figure 6. On the other hand, the RMSE indicates that an average error is committed in the estimation of the irradiation, which is of the order of ± 60 (W/m^2).

7. Artificial Neural Nets to compensate for the absolute temperature dependence

FFNN neural networks are used in adjustment problems, such as the problem studied in this work. An FFNN consists of multiple layers arranged and connected in one direction. The first layer is connected to the input of the network, and each layer is completely connected to the previous. The last layer is connected to the network output. FFNN networks can be used to map any type of input-output relationship.

7.1 ANN architecture and training set

The basic problem is to train an FFNN to estimate the irradiance from the temperature of the cold face, T_C and the open circuit voltage V_{oc} measured by the Pyranometer Peltier (PPLT).

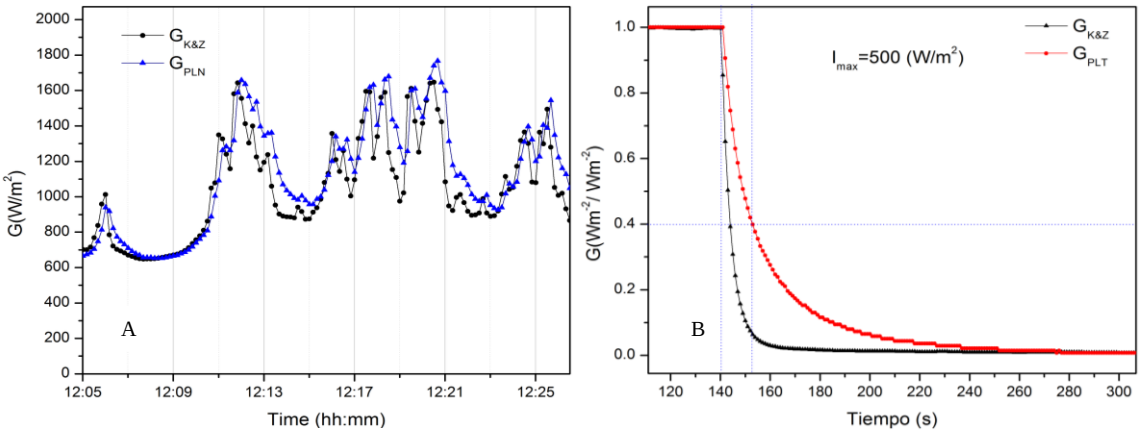

Figure 8. Time delay of the pyranometers. The PPLT is at least 10 seconds slower than the PK&Z, when they are subjected to a fast rafter of $500(\mathrm{W/m^2})$ to 0 $(\mathrm{W/m^2})$.

Using least squares, as indicated in the previous sections, the solar irradiance measured with the PPLT and PK&Z is recorded. The results are shown in Figure 8-A. Note that the blue curve with triangles is delayed, with respect to the black curve with points. To quantify the delay in more controlled conditions, both pyranometers are exposed to the light of an allogeneic lamp, which offers a constant irradiance of 500 (W/m^2). When both pyranometers have a constant output, the lamp is off, and the results are shown in Figure 8-B. The time at which the output of the pyranometers takes 63% of their initial value is calculated. This measurement is known as the Response Time(TR). The results are $TR_{K\&Z} = 2\ (s), TR_{PLT} = 12\ (s)$.

The PPLT takes 10 seconds longer to respond to a change in the irradiance than PK&Z. The reason is that the Peltier cell used as a sensor in the PPLT has more mass and therefore more thermal inertia than the thermopile used as a sensor in the PK&Z.

In this article, two FFNN architectures are proposed, both with a hidden layer and a single exit. The difference is in the number in the FFNN entries and the information in the training set, which includes the delay time. The details are shown next.

7.2 FFNN1

This network consists of a hidden layer, an output and only 2 inputs. The transfer functions are linear for the output layer and sigmoidal for the hidden layer. Its architecture is shown in figure (9), and the network output is calculated according to equation (5).

$$G(t) = f^2(\ \mathrm{LW} \cdot f^1(\mathrm{IW} \cdot \mathrm{P} + \mathrm{b}^1)\ + \mathrm{b}^2) \tag{5}$$

where f^2 and f^1 are the linear and sigmoidal transfer functions, respectively, IW and LW are the synaptic weight matrices of the hidden layer and the output layer, respectively, b^1 and b^2 are the vectors of the trend, and P is the input matrix of the training set. Each element of the training set is presented to the network according to equation (6).

$$P_k^j = P(V_{oc}^j(t + k \cdot \Delta t), T_c^j(t + k \cdot \Delta t)) \qquad G^j = G_{K\&Z}^j(t) \tag{6}$$

where $\mathrm{G^j}$ is a component of the target vector of the training set or the irradiance measured with the PK&Z, k is a whole number in the range $0 \leq \mathrm{k} \leq 5$, and Δt is a constant time interval $\Delta t = 10(\mathrm{s})$.

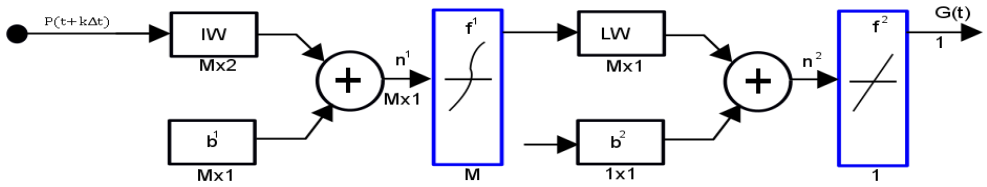

Figure 9. $FFNN1$ architecture with only 2 inputs, temperature T_c from the cold side of the Peltier and the open circuit voltage V_{oc}. There is an irradiance output G_{PLT} and M neurons in the occult layer.

The Input Matrix P_k and the target vector G are shown in equation (7), for a value of k. They form a training set that will be presented to the ANN of M neurons in the occult layer, as shown in Figure 9, where N is the data numbers for V_{oc}, T_c and $G_{K\&Z}$, as measured.

$$P_k = \begin{bmatrix} V_{oc}^1(t + k \cdot \Delta t) & T_c^1(t + k \cdot \Delta t) \\ V_{oc}^2(t + k \cdot \Delta t) & T_c^2(t + k \cdot \Delta t) \\ \vdots & \vdots \\ V_{oc}^N(t + k \cdot \Delta t) & T_c^N(t + k \cdot \Delta t) \end{bmatrix} \qquad \mathbf{G} = \begin{bmatrix} G_{K\&Z}^1(t) \\ G_{K\&Z}^2(t) \\ \vdots \\ G_{K\&Z}^N(t) \end{bmatrix} \tag{7}$$

The number of neurons M in the hidden layer of $FFNN1$ as shown in Figure 9 is in the range $2 \leq M \leq 16$. In other words, 15 $FFNN1$ configurations are trained with 5 different training sets obtained from equation (7) when k is between $0 \leq k \leq 5$

Note that G does not possess index k, unlike P_k. It must be so, because the aim is to compensate for the delay time of the PPLT by providing information to FFNN 1 of $V_{oc}(t + k \cdot \Delta t)$ and $T_c(t + k\Delta t)$, which corresponds to $k\Delta t$ in the 'future' to estimate the current irradiance $G(t)$

Neural networks are trained using the Levenberg-Marquardt algorithm. Some of the statistics, the result of the training of 75 configurations of $FFNN1$, are shown in columns 4 and 5 in table 3, where NNA is an index that indicates one of the configurations. Column 2 indicates the number of neurons in the hidden layer of one of the 75 configurations of $FFNN1$, and the value of $k\Delta t$ indicates the Delay time, which is between 0 and 40 seconds.

Table 3. some of the statistics that result from training the 75 $FFNN1$ configurations

NNA	Neurons in the hidden layer	$k\Delta t$ (s)	MAE	R^2
1	2	0	23.32088	0.9864
2	3	0	23.81246	0.98635
⋮	⋮	⋮	⋮	⋮
15	16	0	26.12485	0.98132
16	2	10	18.6047	0.99171
17	3	10	18.62831	0.99169
⋮	⋮	⋮	⋮	⋮
31	16	10	19.49387	0.99095
⋮	⋮	⋮	⋮	⋮
75	16	40	42.87538	0.95081

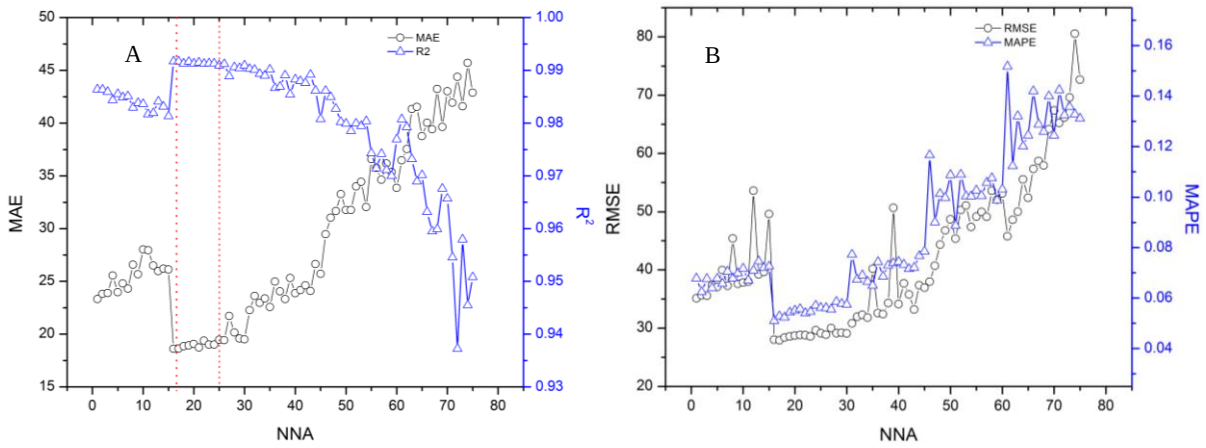

Figure 10. The graphs on the left show the value of the MAE and the R^2 statistics as a function of $k\Delta T$ and the number of neurons in the hidden layer. The $RMSE$ and $MAPE$ statistics are shown on the right, for the 75 trained $FFNN1$ configurations.

The best $FFNN1$ configuration can be chosen by observing the statistics in Figure 10. As mentioned above, each of the 75 configurations are indicated with the NNA index. From the graph, it is clear that statisticians take their best values when NNA is approximately 20. From the notation indicated in Table 5, it is concluded that FFNN with 5 neurons in the hidden layer and a training set. $k = 1$ in $k\Delta t = 10\ (s)$ produces the best results.

7.3 FFNN 2

This neural network consists of a hidden layer, an output and R inputs. The transfer functions are linear for the output layer and sigmoidal for the hidden layer. Its architecture is shown in figure (11), and the network output is calculated according to equation (8).

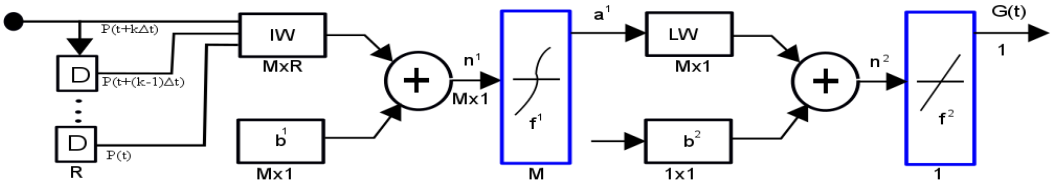

Figure 11. FFNN2 architecture with R temperature inputs, T_c the cold Peltier face, the open circuit voltage V_{oc}, an irradiance output G_{PLT} and M neurons in the occult layer. Note that D represents a temporary delay of the order of $k\Delta$t.

$$G(t) = f^2(\ LW \cdot f^1(IW \cdot P + b^1)\ + b^2) \tag{8}$$

Here, f^2 and f^1 are the linear and sigmoidal transfer functions, **IW** and **LW** are the synaptic weight matrices of the hidden layer and the output layer, $\mathbf{b}^1$ and $\mathbf{b}^2$ are the vectors of trend, and **P** is the input matrix of the training set. Each row of the training set is presented to the network according to equation (9).

$$P_k^j = P(\ V_{oc}(t), T_c(t) \ldots\ldots . V_{oc}(t + k \cdot \Delta t), T_c(t + k \cdot \Delta t)\ ) \qquad G^j = G_{K\&Z}^j(t) \tag{9}$$

Note that in this case, there can be more than one value for V_{oc} and T_c. G^j is a component of the target vector of the training set or the irradiance measured with the PK&Z; k is a whole number in the range $0 \leq k \leq 5$, and Δt is a constant time interval $\Delta t = 5$ (s).

$$\boldsymbol{P_K} = \begin{bmatrix} V_{oc}^{1}(t) & T_c^{1}(t) & \cdots & V_{oc}^{1}(t+k\cdot\Delta t) & T_c^{1}(t+k\cdot\Delta t) \\ V_{oc}^{2}(t) & T_c^{2}(t) & \cdots & V_{oc}^{2}(t+k\cdot\Delta t) & T_c^{2}(t+k\cdot\Delta t) \\ \vdots & \vdots & & \vdots & \vdots \\ V_{oc}^{N}(t) & T_c^{N}(t) & \cdots & V_{oc}^{N}(t+k\cdot\Delta t) & T_c^{N}(t+k\cdot\Delta t) \end{bmatrix} \qquad \boldsymbol{G(t)} = \begin{bmatrix} G_{K\&Z}^{1}(t) \\ G_{K\&Z}^{2}(t) \\ \vdots \\ G_{K\&Z}^{N}(t) \end{bmatrix} \tag{10}$$

The Input Matrix $\mathbf{P_k}$ of the training set equation (10) consists of N input vectors P_k^j. The number of components of this vector is R, and the dimension of the input matrix $\boldsymbol{P_k}$ is $N \times R$. The value of R depends on k; for example, if $k = 0$, in that case $R = 2$, and the input matrix would have a size of $N \times 2$. If $k = 1$, in that case $R = 4$, and the input matrix $\mathbf{P_k}$ would be the size of $N \times 4$, unlike the training set for FFNN1, in which the input matrix is always the same size. N $\times$ 2, the size of the input matrix for FFNN2, depends on the value of k.

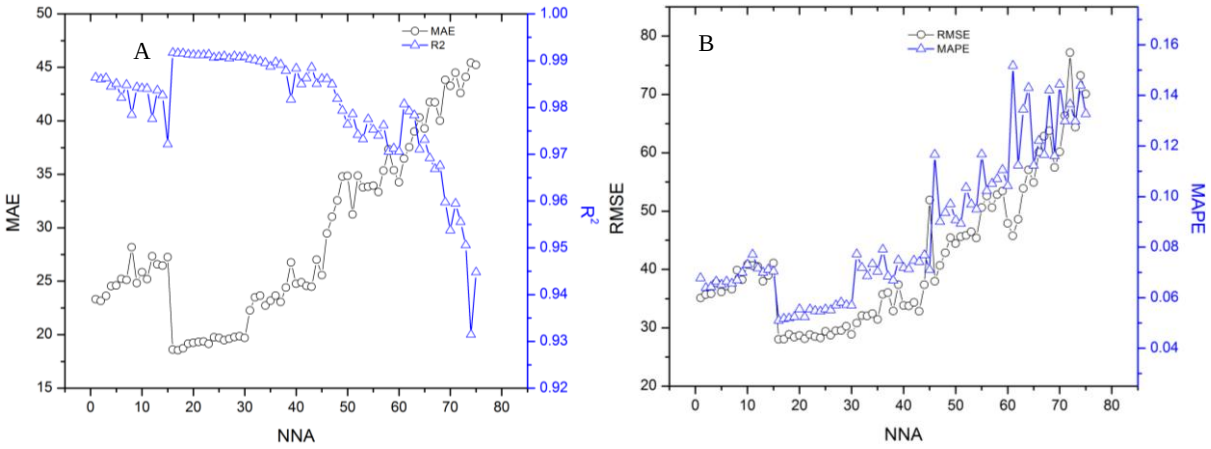

Figure 12. The graphs on the left show the value of the MAE and the R^2 statistics as a function of $k\Delta T$. The number of neurons in the hidden layer, the $RMSE$ and $MAPE$ statistics are shown on the right, for the 75 trained $FFNN_2$ configurations.

Neural networks are trained using the Levenberg-Marquardt algorithm. The results of the FFNN2 training are shown in Figures 12-A and 12-B, where the statistics are plotted against the NNA index, which indicates one of the 75 FFAA2 configurations that result from varying the number of neurons in the hidden layer and varying k in the input matrix of the training set.

8. Conclusions

In this work, a low-cost pyranometer was constructed and evaluated using a commercial Peltier cell TEC-12705 as a thermoelectric generator. In the designed instrument, the open circuit voltage and the cold face temperature in the Peltier are measured, using multiple regression to a plane and two neural network architectures to estimate the irradiance from the measured values.

The results are compared with one of the best thermopile pyranometers available on the market, using 4 statistics that measure the performance of our pyranometer compared to the KPP & ZONEN CMP22.

Observing Figures $10-A, 10-B, 12-A$ and $12-B$, it is concluded that the best results in both configurations of FFNNs are around the configuration indicated with $ANN = 20$, which correspond to an FFNN of 5 neurons in the hidden layer and a training set constructed with $ak = 1$. These indicate to include, in the network training, the cold face temperature information T_c and open circuit voltage V_{oc} 10 seconds before estimating the irradiance.

Table 4. Comparison of the PPLT performance against PK&Z.

	MAE	**RMSE**	R^2	**MAPE**
	(Wm^{-2})	$Wm^{-2})$	--	%
Minimal Squares	27.1993	54.7348	0.9647	0.07443
$FFNN1$	19.00957	28.66784	0.99129	0.05594
$FFNN2$	18.97250	28.47851	0.99128	0.05450

The results in terms of 4 statistics commonly used to measure performance are shown in Table 4. It is observed that the two proposed FFNN configurations work better than the least squares procedure.

All of the statistics used show that of the two tested neural network configurations, $FFNN2$ is slightly higher than the $FFNN1$ configuration.

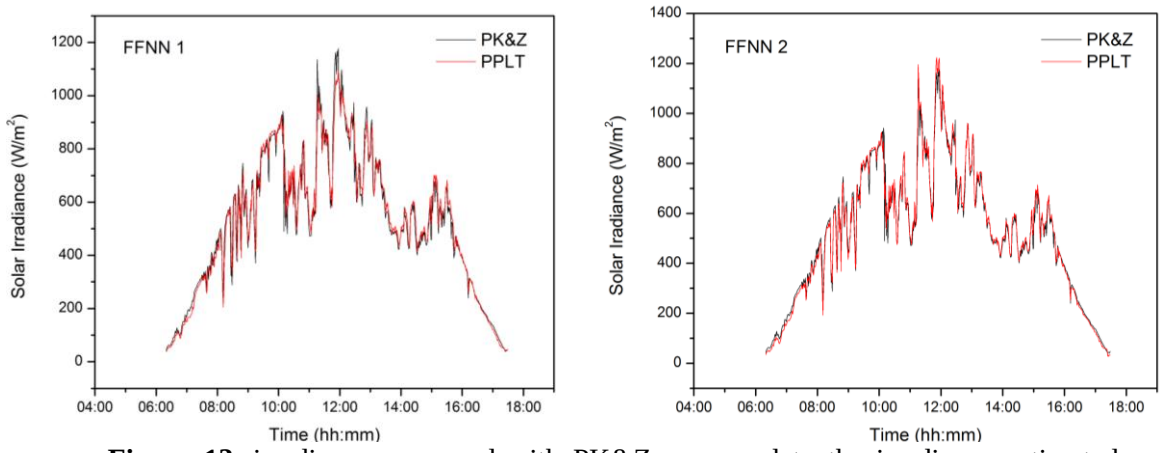

Figure 13. irradiance measured with PK&Z compared to the irradiance estimated with PPLT for the two tested FFNN configurations.

Figure 13 shows the results of the measurement of solar irradiance on a partly cloudy day; you can see the performance of the two configurations of $FFNN$ against the $CMP22\ KIPP\ \&\ ZONEN$ pyranometer. In the figures, from observing the maximum irradiance values, it is evident that the $FFNN_2$ configuration is slightly higher than the $FFNN1$ configuration.

Acknowledgments
Thanks to the Universidad Nacional de San Agustín de Arequipa for financing the basic and applied research project "Energy efficiency in photovoltaic systems with artificial neural networks that include losses due to the accumulation of dust in arid climates" with contract No. IBA-0033- 2016.

References

[1] Pelland S, Remund J, Kleissl J, Oozeki T and Brabandere K 2013 Photovoltaic and solar forecasting: state of the art report *International Energy Agency IEA* (Report IEA PVPS T14-01:2013) p 22
[2] Gauntlett D 2013 Solar PV market forecasts *Navigant Consulting, Inc.* (Chicago IL USA Tech.)
[3] Zhang Y, Beaudin M, Taheri R and Zareipour H 2015 Day-ahead power output forecasting for small-scale solar photovoltaic electricity generators *IEEE Trans. Smart Grid*, vol 6 pp. 2253-62

[4] Hong T, Pinson P and Fan S 2014 Global energy forecasting competition 2012 *International Journal Forecasting*
[5] Hong T, Pinson P, Fan S, Zareipour H, Troccoli A and Hyndman R 2014 Probabilistic energy forecasting: global energy forecasting competition 2014 and beyond *International Journal Forecasting*
[6] Letendre S, Makhyoun M and Taylor M, 2014 Predicting solar power production: irradiance forecasting models, applications and future prospects *SEPA solar electric power association*
[7] Dieterink B 2010 CMP serie piranómetro 1007 AH Delft Holanda (www.kippzonen.com) p 15
[8] Carrasco M, Laudani A, Lozito G, Mancilla F, Riganti F and Salvini A 2017 Low-cost solar irradiance sensing for PV systems *MDPI energies*
[9] Mancilla F Riganti F, Laudani A, and Salvini A 2013 A neural network-based low-cost solar irradiance sensor *IEEE transactions on instrumentation and measurement*. vol 63 0018-9456 © 2013 IEEE
[10] Vignola F, Derocher Z, Peterson J, Vuilleumier L, Felíx C, Grobner J and Kouremeti N 2016 Effects of changing spectral radiation distribution on the performance of photodiode pyranometers *Solar energy* vol 129 pp 224-35
[11] Sousa I, Oliveira R, Medeiros C and Silva E 2018 Estimation of global solar irradiance with LDR sensor and artificial neural network embedded in an 8-bit microcontroller *IEEE Int Joint Conference on neural networks* (IJCNN)
[12] Lineykin S and Ben S 2007 Modeling and analysis of thermoelectric modules *IEE Transactions on Industry Applications* vol 43 No 2
[13] Soberanes G 2017 Determination of seebeck coefficient in a commercial peltier cell *Congreso Int. Internacional de Investigación Academia Journals Fresnillo* vol 9 No 1
[14] Vargas J and Flóres A 2016 Implementation of the peltier cell in waste heat sources, to take advantage of electric power generation and cold air conditioning in the home *VISIÓN-Revista de Investigaciones UNICIENCIA* vol2 No 2 pp 62-69
[15] Pottier N 2007 Static physics excluding d'équilibre irreversible linear processes *Current Knowledge EDP Sciences/CNRS Editions* Paris France pp 63-72
[16] Arias J 2005 Non-equilibrium thermodynamics in small systems *Instituto madrileño de estudios avanzados en nanociencia* (IMDEA)
[17] Seifert W, Ueltzen M and Müller E 2002 One-dimensional modelling of thermoelectric cooling *phys. Stat. sol*. 194 No 1 pp 277-90
[18] Despotovic M, Nedic V, Despotovic D and Cvetanovic S 2015 Review and statistical analysis of different global solar radiation sunshine models. *Renewable and Sustainable Energy Reviews* 52 pp 1869–80
[19] Wilamowski B 2009 Neural network architectures and learning algorithms *IEEE Ind. Electron. Mag* vol. 3, no. 4, pp. 56–63